PROCEEDINGS, 51st Workshop on Geothermal Reservoir Engineering
Stanford University, Stanford, California, February 9-11, 2026
SGP-TR-230

Rayleigh-Frequency-Shift Distributed Strain Sensing (RFS-DSS) of Huff-Puff Tests Conducted at Utah FORGE

Ghoulem Ifrene, Matthew W Becker, Dana Jurick and Artur Guzik

California State University, Long Beach, Geology Department, 1250 Bellflower Boulevard, Long Beach, California, 90840, USA

ghoulem.ifrene@csulb.edu , Matt.Becker@csulb.edu

Neubrex Energy Services (US), LLC

dana.jurick@neubrex.com

Neubrex Infra AG, Badstrasse 4, Baden, Switzerland

guzik@neubrex.com

Keywords: Rayleigh DSS, DTS, near-wellbore compliance, Utah FORGE, cyclic injection, huff-puff tests, EGS, DFOS

ABSTRACT

Huff-puff (cyclic injection/flowback) tests can provide comparatively rapid hydraulic and tracer responses compared to cross-well testing. In August of 2025, we executed a huff-puff diagnostic test at the Utah FORGE well 16B(78)-32 and collected a rich multi-sensor dataset. Fiber-optic cable housed in 4.4 cm diameter steel coiled tubing installed in the cased hole provided Rayleigh frequency shift distributed strain sensing (RFS-DSS), together with distributed temperature sensing (DTS) and distributed acoustic sensing (DAS). Three rate steps (2.5, 5.0, 7.5 bpm) produced repeatable DSS responses concentrated near perforated intervals. DSS responses at perforations may be due to changes in temperature, strain, or both. Decoupling thermal and mechanical signatures requires joint analysis of DSS and DTS. In addition, the transfer of both heat and strain through the coiled tubing requires additional consideration. Nevertheless, these tests indicate that it is possible to identify flow exchange during huff-puff tests using an intervention fiber installation in coiled tubing. Quantitative analysis and workflow development are underway.

1. INTRODUCTION

Enhanced Geothermal Systems (EGS) are a key pathway for expanding geothermal power beyond naturally permeable hydrothermal resources, but they depend on creating and sustaining effective fluid pathways in hot, low-permeability rock. As a result, field-scale EGS development relies upon diagnostics that can rapidly identify where the reservoir is exchanging fluid and heat with the wellbore and how those pathways evolve during stimulation and subsequent operations.

Single-well cyclic injection/flowback ("huff-puff") tests offer an operationally efficient way to probe near-wellbore transport and exchange without the logistical and cost overhead of dedicated multi-well campaigns (Pruess, 2010). Because the induced flow field is reversed during withdrawal, huff-puff tests can reduce sensitivity to advective heterogeneity and sharpen inference on diffusive exchange and heat-transfer behavior, making them attractive for fractured geothermal settings (Ghergut et al., 2007).

Utah FORGE provides an unusually well-instrumented and publicly documented testbed to advance these diagnostics (Figure 1). At FORGE, fiber-optic monitoring has already been used to support interval selection and to map inflow behavior via thermally driven signals during post-stimulation circulation and stimulation activities (Ajo-Franklin et al., 2025; Ratnayake & Ghassemi, 2023; Xing et al., 2025). Distributed fiber-optic sensing (DFOS) can deliver meter-scale, continuous measurements along the wellbore, combining distributed temperature sensing (DTS), distributed acoustic sensing (DAS), and distributed strain sensing (DSS), has become a widely adopted monitoring approach across subsurface energy and storage applications (Liu et al., 2024).

A distributed strain sensing (DSS) system uses a fiber-optic interrogator to inject laser light into an optical fiber and analyze the backscattered signal returning from natural in-fiber scatterers. By tracking how the backscatter signature changes along the cable, the interrogator estimates axial deformation of the fiber as a function of depth (or distance) and time. In practice, each reported "measurement point" is not truly infinitesimal, the instrument reports strain that is effectively averaged over a finite window along the fiber. The length of that averaging window is commonly called the gauge length (and it strongly influences spatial smoothness and noise). Longer gauge lengths generally improve signal-to-noise but smear sharp, localized features; shorter gauge lengths improve localization but can be noisier.

DSS measures one-dimensional (axial) strain along the fiber, i.e., how much the fiber's displacement changes from one location to the next (Equation 1). Using the basic definition of normal strain, the axial strain associated with sensing index i can be written as a finite difference of displacement over the gauge length L (Ratnayake & Ghassemi, 2023):

$$\varepsilon_{xx}^{i} = \frac{u_x^i - u_x^{i+1}}{L} \tag{1}$$

where u_x^i and u_x^{i+1} are the axial displacements at two locations separated by the gauge length L. Because DSS data are recorded in time, it is often useful to work with the strain rate, defined as the time derivative of strain (Equation 2). In discrete form, for time steps t^n and t^{n+1}.

$$\dot{\varepsilon}_x = \frac{d\varepsilon_x}{dt} = \frac{\varepsilon_x^{n+1} - \varepsilon_x^n}{t^{n+1} - t^n} \quad (2)$$

x denotes the fiber axis, i indicates spatial index (sensing location), and n denotes the time index.

Extracting mechanically meaningful information from Rayleigh-based DSS is non-trivial because Rayleigh Frequency Shift (RFS-DSS) observables are sensitive to both strain and temperature (Zhou et al., 2013). This relationship can be expressed as:

$$\Delta\nu_R = C_{21}\,\Delta\varepsilon_x + C_{22}\,\Delta T \quad (3)$$

where $\Delta\nu_R$ is the Rayleigh frequency shift for a given fiber segment, $\Delta\varepsilon_x$ is the axial strain change, ΔT is the temperature change, and C_{21} and C_{22} are calibration coefficients that depend on the fiber type and also sensing cable design and manufacturing (Ugueto et al., 2021). As a result, observed "strain" anomalies during thermal transients may reflect thermo-elastic or glass refraction index effects rather than true formation deformation, motivating workflows that explicitly leverage DTS to constrain temperature contributions before interpreting any residual as mechanical.

In this study, we report field observations from a huff-puff diagnostic campaign conducted in August 2025 at Utah FORGE well 16B(78)-32 (Figure. 1). Fiber-optic cable housed in coiled tubing (CT) installed in the cased hole provided Rayleigh frequency-shift DSS (RFS-DSS), together with DTS and DAS. The test program included multiple cyclic injection/flowback steps, including rate steps at 2.5, 5.0, and 7.5 bpm. Across these steps, DSS responses concentrate repeatably near perforated intervals, consistent with localized exchange during injection and backflow.

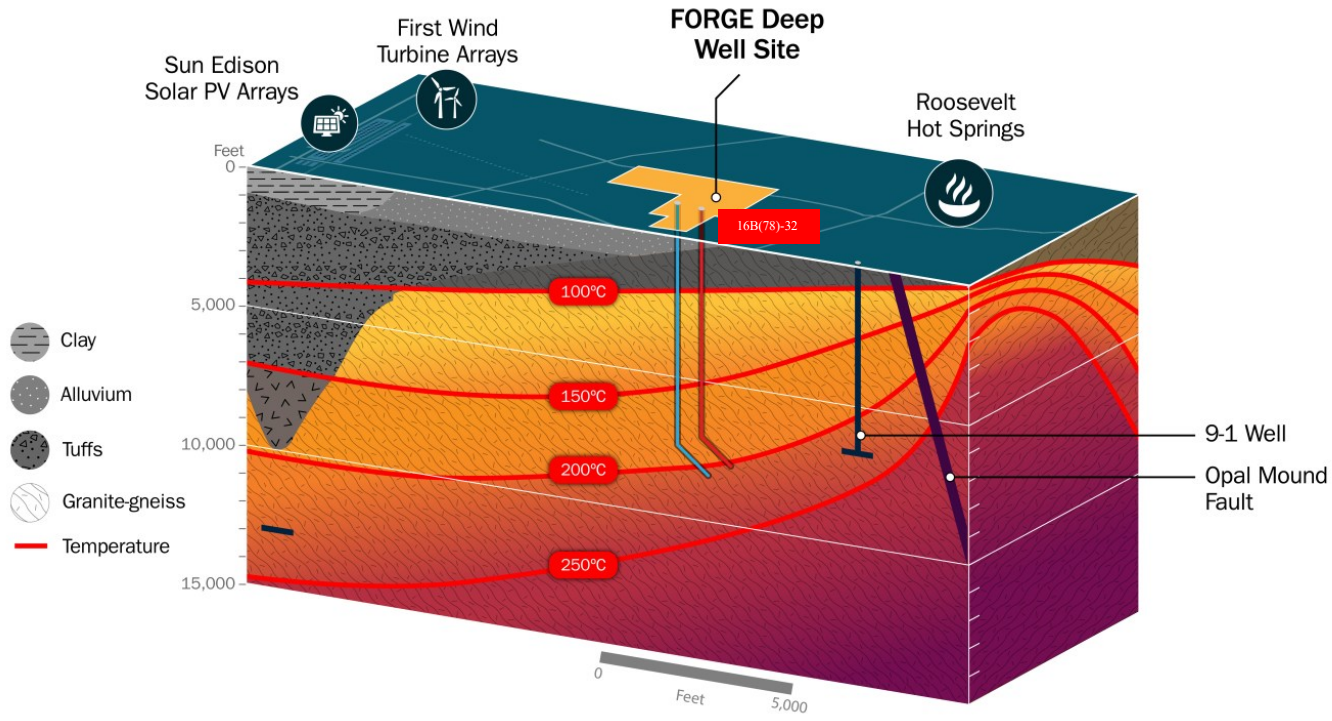

Figure 1:The locations of the 16B(78)-32 geothermal well used in this study, modified from (*Department of Energy*, 2023)

The primary objective of this paper is to communicate what RFS-DSS can (and cannot) robustly reveal about near-wellbore behavior during cyclic operations in an intervention-fiber coiled-tubing (CT) configuration .We frame the interpretation around joint analysis of DSS and DTS to separate temperature-driven components from any residual elastic response, while also acknowledging that temperature and strain cross-sensitivity requires explicit treatment when both fields evolve simultaneously (Pedraza et al., 2023). We further note that heat and strain transfer through the coiled-tubing and cable packaging can introduce delayed temperature response and slippage that must be accounted for before claiming formation-mechanical attribution (LeBlanc et al., 2025; Song et al., 2024). The results support the use of intervention RFS-DSS in CT as a practical, high-resolution diagnostic for identifying flow exchange during huff-puff tests, and they

highlight key requirements for defensible mechanical inference in future deployments (Ghergut et al., 2007; Pruess, 2010; Schölderle et al., 2023).

2. TEST DESIGN AND OPERATIONS

Figure 2 shows the surface arrangement for the huff-puff campaign. The 16B wellhead and 16A wellhead are positioned on the central portion of the pad, with JB0-JB1-JB2 junction boxes providing telemetry for the FO. A geothermal separator sits between the wells and the sump to manage produced water and steam during flowback.

Water handling and pumping are organized on the south sides of the pad. A large sump occupies the northwest quadrant for temporary flowback storage. Treated water is staged in the Minion tank with a booster pump and a water-treatment trailer upstream of the pressure-pumping spread. Three pump trucks are lined up south of the wells, oriented so that the discharge lines can be routed directly to the wellhead through a pressure-control package. A dedicated "calibration line" is used for instrument or flow calibrations without interfering with main injection/return paths. The planned fiber-optic conduits run from the wellhead area toward the junction boxes (JB0, JB1 and JB2), providing a clear, protected path for the CT-deployed fiber.

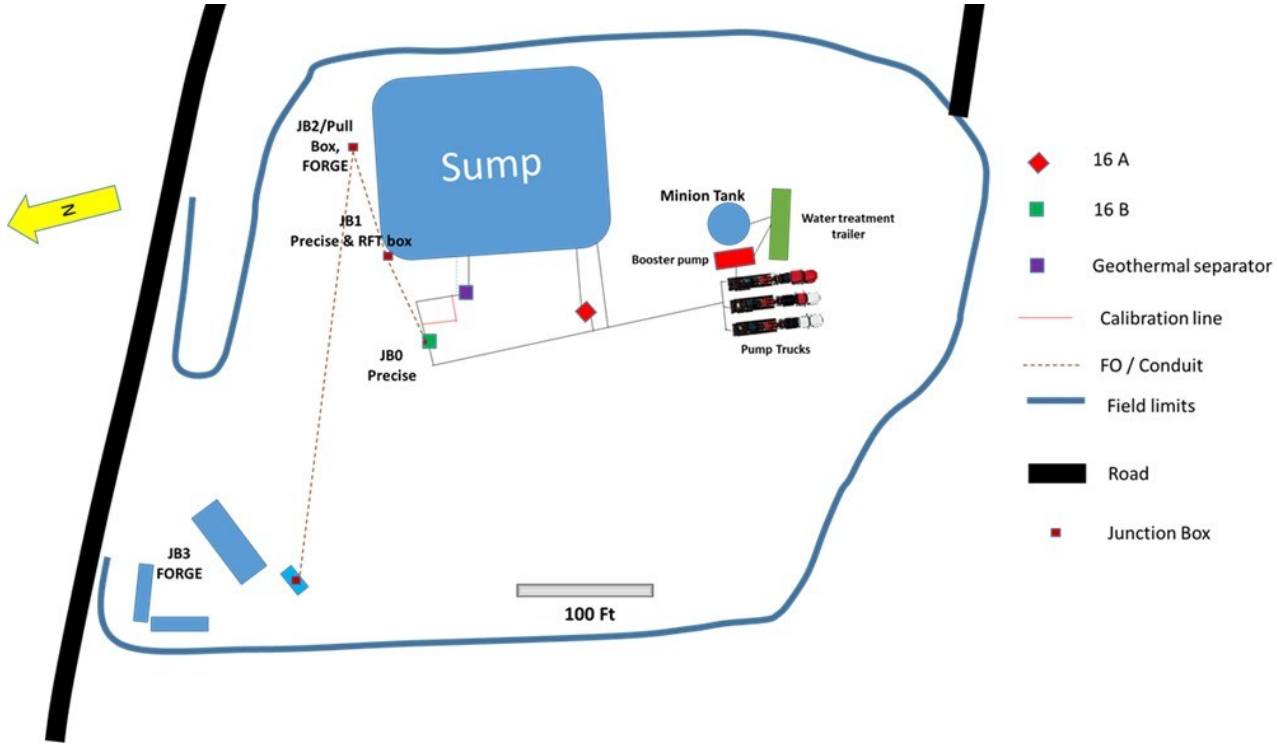

Figure 2: Site footprint for the Huff Puff test

The surface rig-up routed fresh water from the Minion tank and booster through the pressure-pumping spread to 16B via a dedicated injection line. Immediately downstream of the wellhead two isolation valves provided the primary means to shift between injection and flowback; this arrangement let pumping-services personnel control the huff-puff sequence while keeping adjustable chokes away from the wellhead for safety and fine rate control (Figure 3). During flowback, returns passed through the choke where rate pressure was measured, then to the geothermal separator before going to the sump. Surface data (flow, temperature, pressure) were logged continuously while the DTS/DAS/DSS are collected throughout the operation.

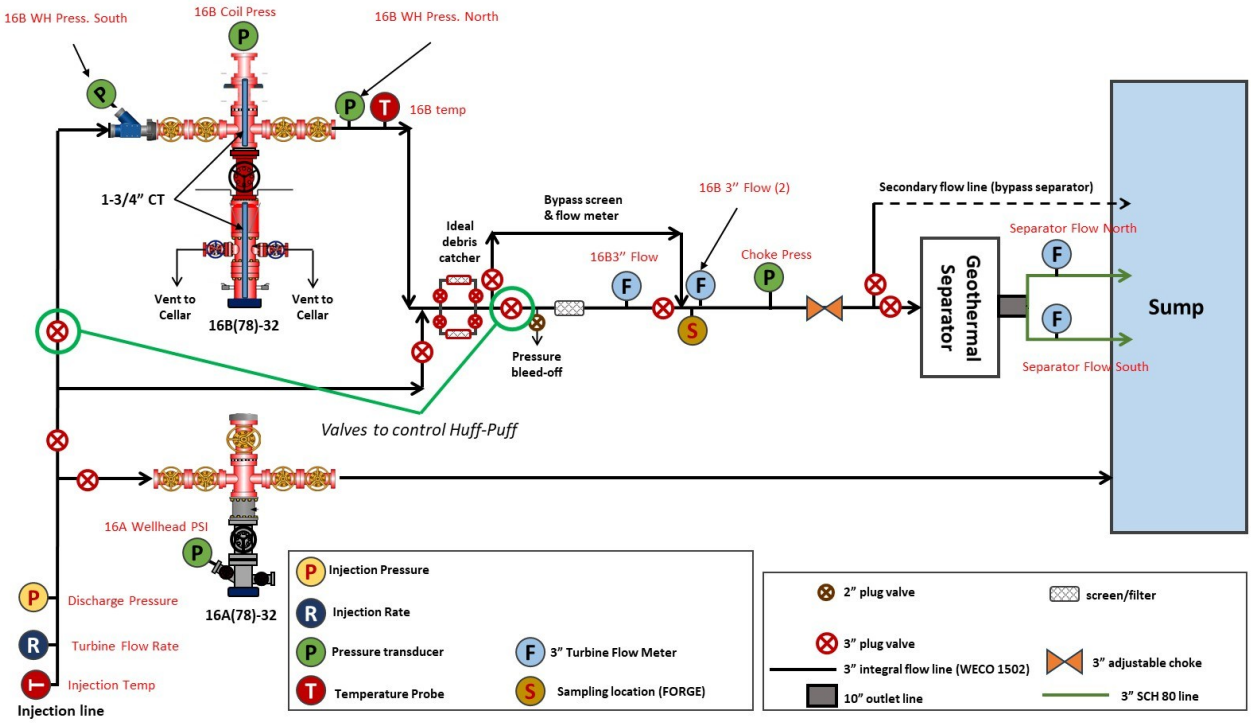

Figure 3:Huff puff surface injection system

Utah FORGE's well 16B(78)-32 is a highly deviated bore (65 °) that parallels the injector 16A(78)-32 at roughly 300 ft offset; it was completed to about 10,947 ft measured depth (~8,262 ft TVD) with stimulation focused across ~800 ft in five stages to create connectivity for an EGS circulation loop. Perforations for stimulation and exchange are concentrated between 9800 and 8850 MD and grouped into five stages (S1-S5) with multiple perforation clusters per stage (C1-C4), as shown on the casing/perforation schematic (Figure. 4a).

For the huff-puff campaign, we ran a 4.4 cm-OD steel coiled-tubing (CT) string inside the casing; the CT housed the fiber-optic bundle and auxiliary lines (Figure 4c): a dedicated single-mode fiber for Rayleigh-based distributed strain sensing (DSS), a single-mode fiber for DAS and a multi-mode fiber for DTS, in 0.6 cm-OD capillary tubes, and a pressure-sensing conduit line (Figure 4b). The CT followed the well path, ensuring that the fibered measurements sampled the same perforated intervals targeted by the test and minimizing uncertainty in depth registration across the distributed measurements.

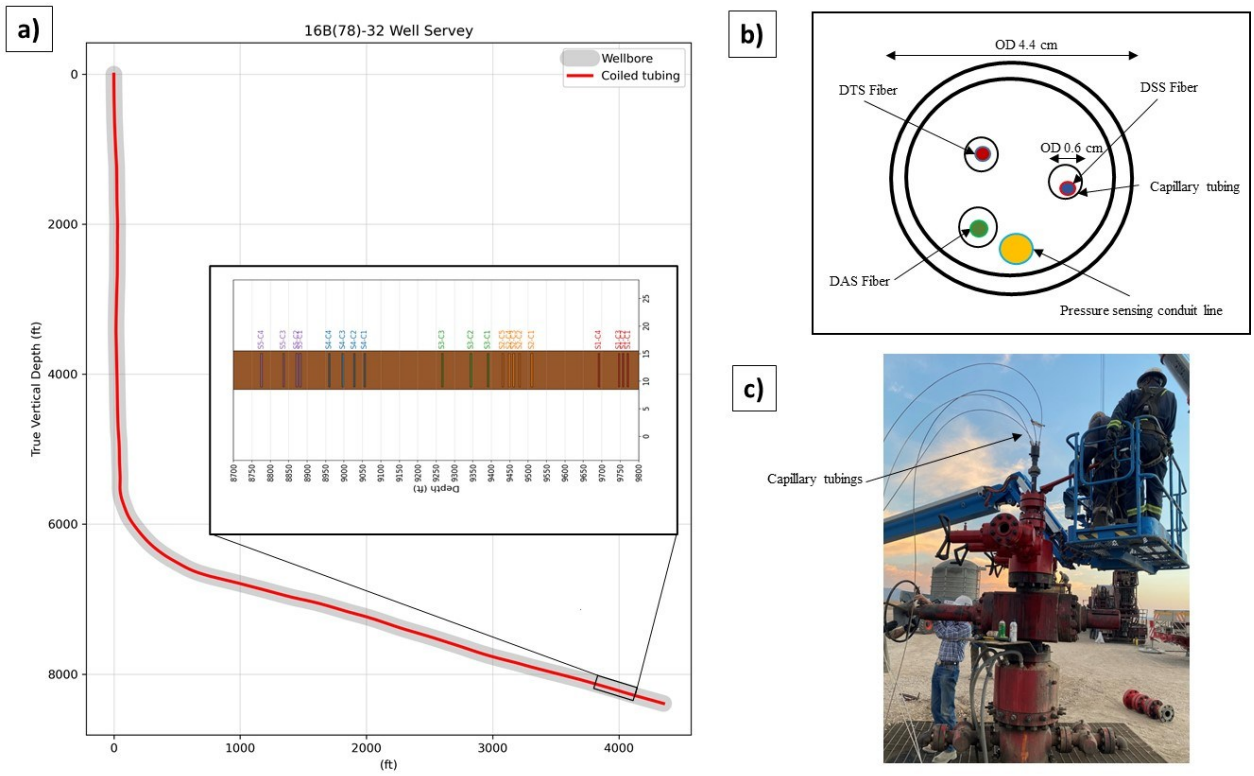

Figure 4: 16B(78)-32 well trajectory and CT-based DFOS installation a) Well survey showing the wellbore trajectory b) Schematic of the CT cross-section, c) field photo of the wellhead showing the capillary lines

Huff-puff tests were designed to injection solute tracers which are not discussed in this article. Injection was planned to first displace the annular water volume outside the CT (~340 bbl.), after which injection proceeded at the target step rates. Flow was controlled using surface pump trucks; each injection was followed immediately by flowback. Because of chase-water volumes, planned flowback volumes exceeded injection volumes. The program comprised five huff-puff cycles with defined step rates, durations, and chase-water periods. The design included rate steps at 2.5 and 5 bpm and allowed a high-rate step at 7.5 bpm; corresponding flowback durations were set to exceed injection durations to account for chase-water recovery (Table 1).

Table 1: Huff Puff Tracer Testing Activities

Pumping Activity	Rate (bpm)	Total Inj Time (min)	Tot Inj Volume (bbl.)	Return Vol (bbl.)
Injection 1: Tracer 1	2.5	200.0	500	
Flowback 1	2.5			620
Injection 2: Tracer 2	2.5	278.0	695	
Flowback 2	2.5			920
Injection 3: Tracer 3	2.5	353.0	883	
Flowback 3	2.5			1220
Injection 4: Tracer 4	5	131.5	658	
Flowback 4	5			620
Injection 5: Tracer 5	7.5	70.8	531	
Flowback 5	6.75			693
Totals			3266	4073

In addition, three short pulses have been added to the test as described in table 2.

Table 2: Short pulses

Pumping Activity	Rate (bpm)	Inj/Ret Duration (min)	Inj Vol (bbl.)	Ret Vol (bbl.)
Pulse 1: Inject	2.5	5	13	
Pulse 1: Flow	2.5	5		13
Pulse 2: Inject	2.5	10	25	
Pulse 2: Flow	2.5	10		25
Pulse 3: Inject	2.5	15	37	
Pulse 3: Flow	2.5	14		35

Figure 5 summarizes the key surface measurements over the test interval (Aug. 26–29) for the five huff-puff cycles. The top panel compiles the injection pressure, which reveals the transitions between injection, shut-in, and flowback periods across cycles. The bottom panel presents the injection rate and flowback rate (bpm), Showing the imposed step-rate structure during injection and the onset and duration of the injection and flowback phases.

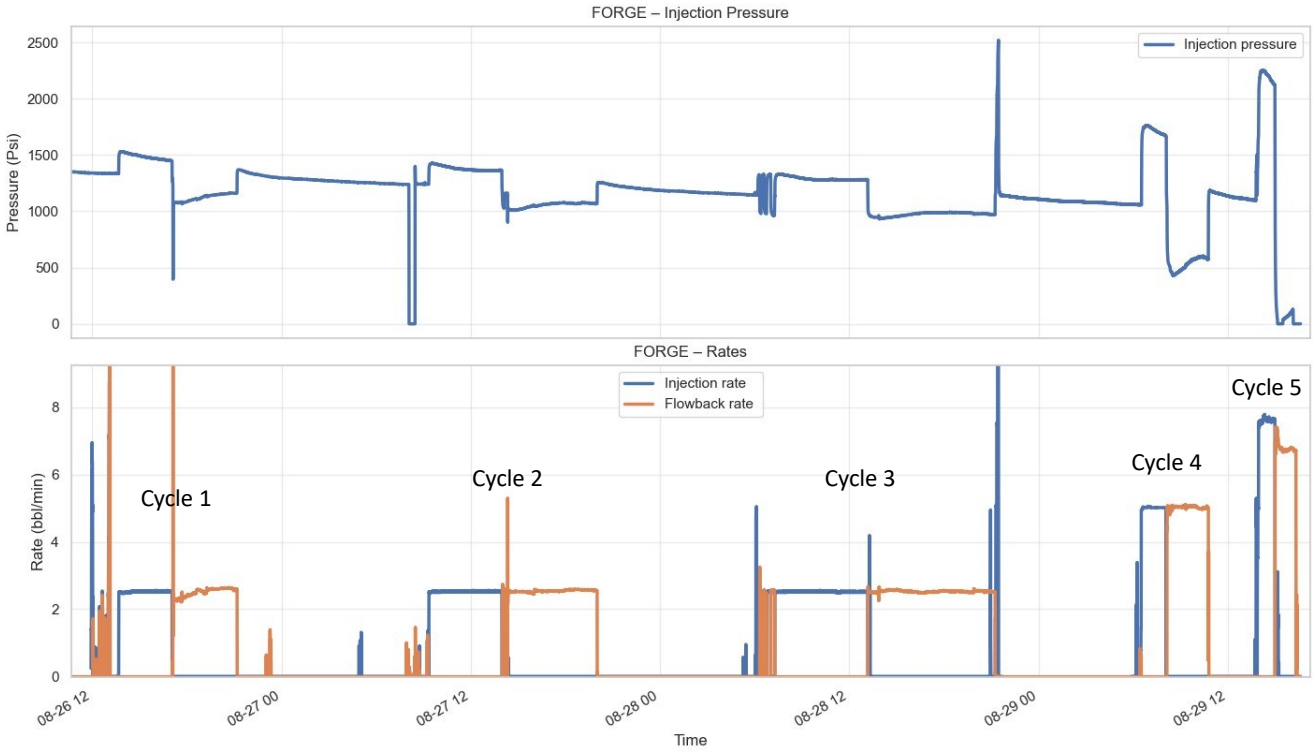

Figure 5: Surface data summary for the Utah FORGE huff puff cyclic test

3. DATA PROCESSING AND ANALYSIS WORKFLOW

The distributed strain sensing (DSS) strain-change rate and distributed temperature sensing (DTS) temperature datasets were imported from HDF5 files and preprocessed to ensure consistent sampling and alignment. Both datasets were referenced using a fixed time offset to place them in a common reference frame, and the analysis was restricted to the time interval where DSS and DTS overlap. To reduce computational load while preserving the relevant temporal trends, the time series were optionally decimated prior to further processing.

Because DSS and DTS are acquired on different depth and time grids using two independent fibers within the CT, the DTS temperature field was mapped onto the DSS grid. Here, RFS-DSS provides 20 cm spatial resolution with 32 s temporal sampling, while DTS provides 100 cm spatial resolution with 35 s per profile. Temperature was first interpolated onto the DSS depth channels and then interpolated onto the DSS timestamps, producing a temperature matrix directly comparable to the DSS strain change and strain-rate at each time-depth sample. The analysis was subsequently limited to the simulated and perforated section of the cased borehole. A smoothed temperature time series was used to compute the temperature first order time-derivative. After moving-average smoothing in time, the derivative $\dot{T}(t,z)$was computed on the DSS time base so that temperature-rate and strain-rate were expressed consistently in the same time units.

Thermal-mechanical decoupling was performed using a linear regression of strain rate (measured by RFS-DSS) and temperature rate (measured by DTS) (Equation 4). Perforation depth intervals were excluded (with an additional depth buffer) to avoid large rate changes

that may be affected by sample interpolation. Using only these reference depths, the temperature influenced apparent DSS strain-rate was modeled as

$$\dot{\varepsilon}_x(t,z)_{apparent} = k(z)\,\dot{T}(t,z) + b(z) \tag{4}$$

where $k(z)$ represents the depth-dependent thermal sensitivity and $b(z)$ accounts for residual bias. Model parameters were estimated using a regression to reduce sensitivity to outliers (Figure 6), either as a single global fit applied across depth or as depth-binned fits subsequently interpolated to obtain continuous $k(z)$ and $b(z)$ profiles.

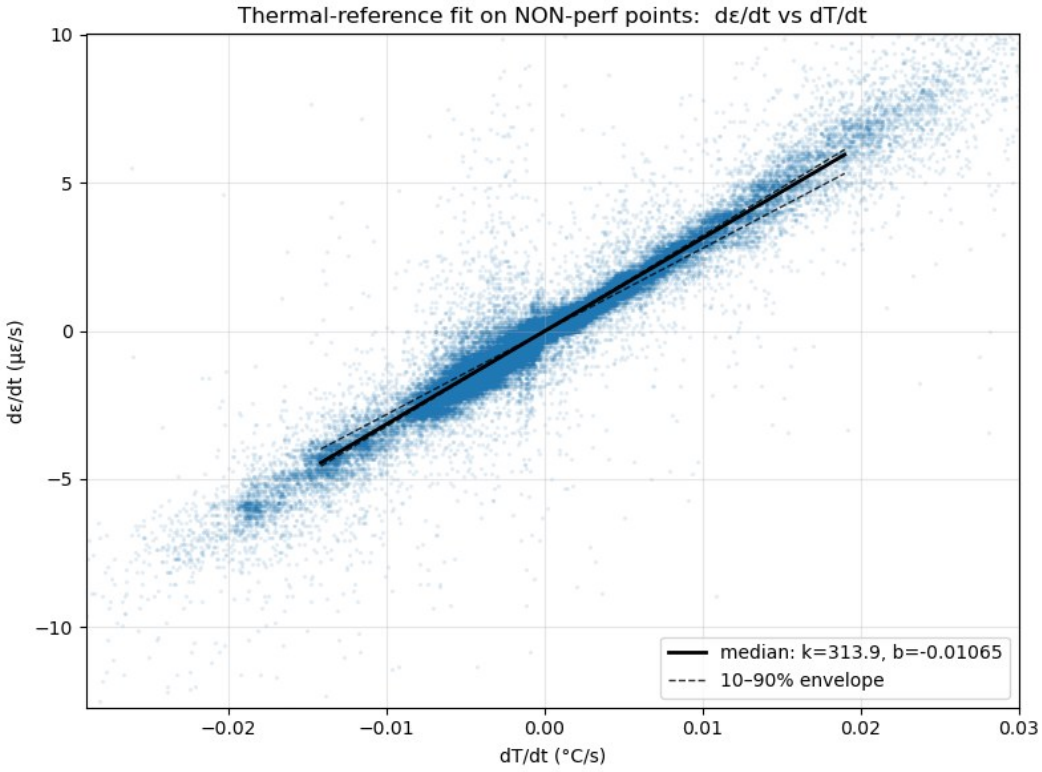

Figure 6: Regression of strain rate (measured by RFS-DSS) versus temperature rate (measured by DTS) for non-perforated depths.

The mechanical strain-rate component was computed as the residual after subtracting the calibrated thermal contribution from the measured strain rate (Equation 5):

$$\dot{\varepsilon}_{x\,\mathrm{mech}}(t,z) = \dot{\varepsilon}_x(t,z)_{meas} - \dot{\varepsilon}_x(t,z)_{apparent} = \dot{\varepsilon}_x(t,z)_{meas} - \left[k(z)\,\dot{T}(t,z) + b(z)\right]. \tag{5}$$

To further suppress acquisition-wide common-mode artifacts, a time-dependent depth-median offset was removed from the residual field, improving the interpretability of localized features.

4. RESULTS

The Rayleigh Frequency Shift Distributed Strain Sensing (RFS-DSS) dataset exhibited excellent signal quality, but the measured strain change rate response was dominated by temperature effects. Temperature changes produce apparent strain due to thermal elongation and change in the refractive index (Sidenko et al., 2022). Under huff-and-puff conditions, both temperature and deformation can be large and highly dynamic, which makes the separation of thermal and mechanical contributions particularly challenging. The result of an attempt to remove the effects of thermal changes on strain measurements using the regression between strain rate and temperature rate (Figure 6) and Equation (5) is shown in Figure 7. The residual mechanical strain produced through this process is an order of magnitude smaller

than the measured strain (Figure 7d). Consequently, if there is an influence of true mechanical strain on the RFS-DSS response, it is small compared to the influence of temperature change.

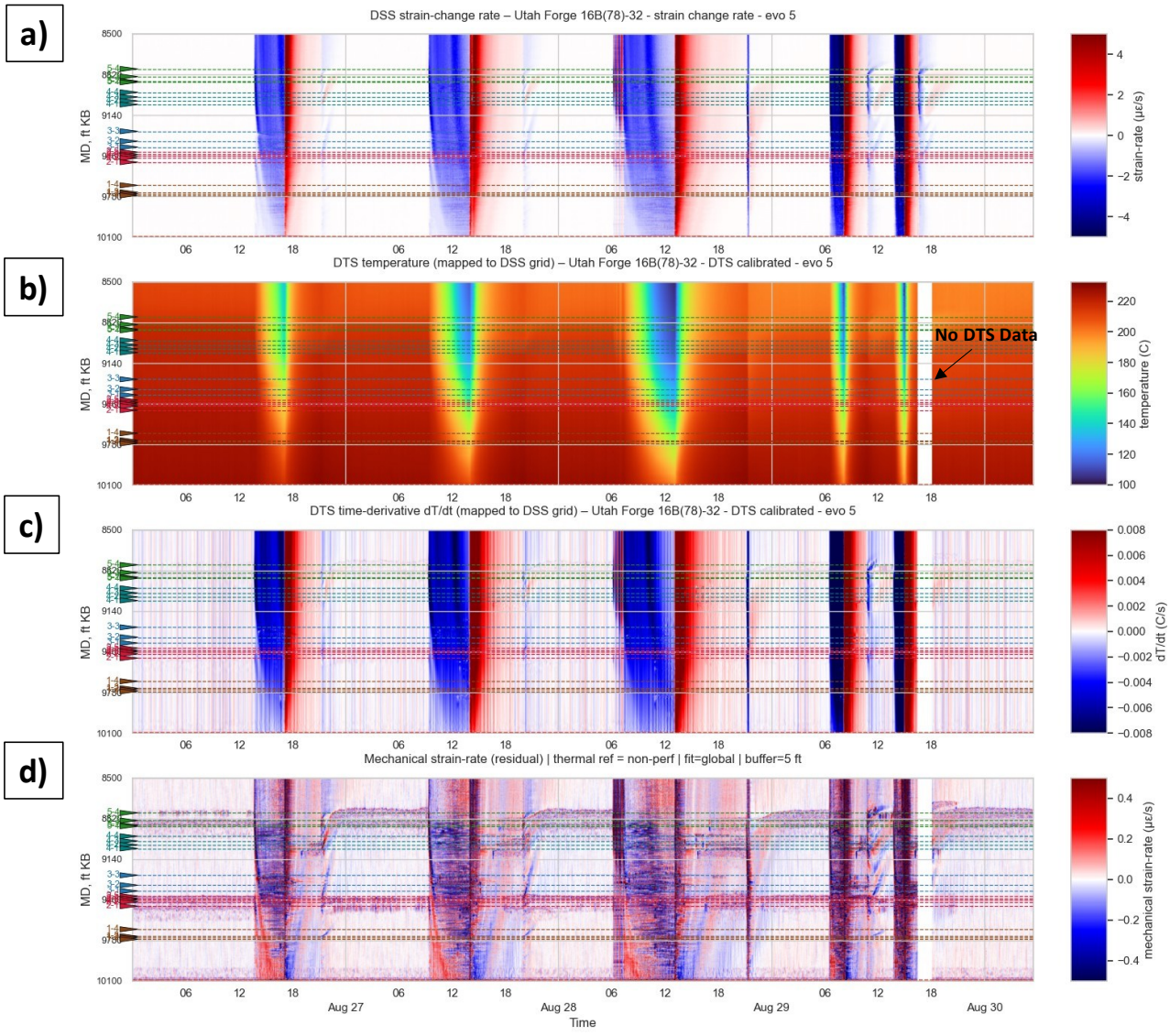

Figure 7:Top to bottom (a) the measured DSS strain-change rate, (b) the DTS temperature mapped to the DSS grid, (c) the temperature time-derivative, and (d) the decoupled mechanical response

The mechanical strain residual (Figure 7d) suggests that mechanical strain may occur during periods of shut in. However, this residual could not be confidently interpreted as true mechanical strain (e.g., fracture displacement) due to CT structure and deployment inside of casing, isolating the sensing fiber from reservoir. Signatures of apparent mechanical strain tend to coincide with rapid changes in temperature where sampling density differences between RFS-DSS and DTS may create artifacts. The tendency for apparent mechanical strain to occur during rapid temperature changes is also apparent in line-plots (Figure 8) extracted from the waterfall plot (Figure 7d).

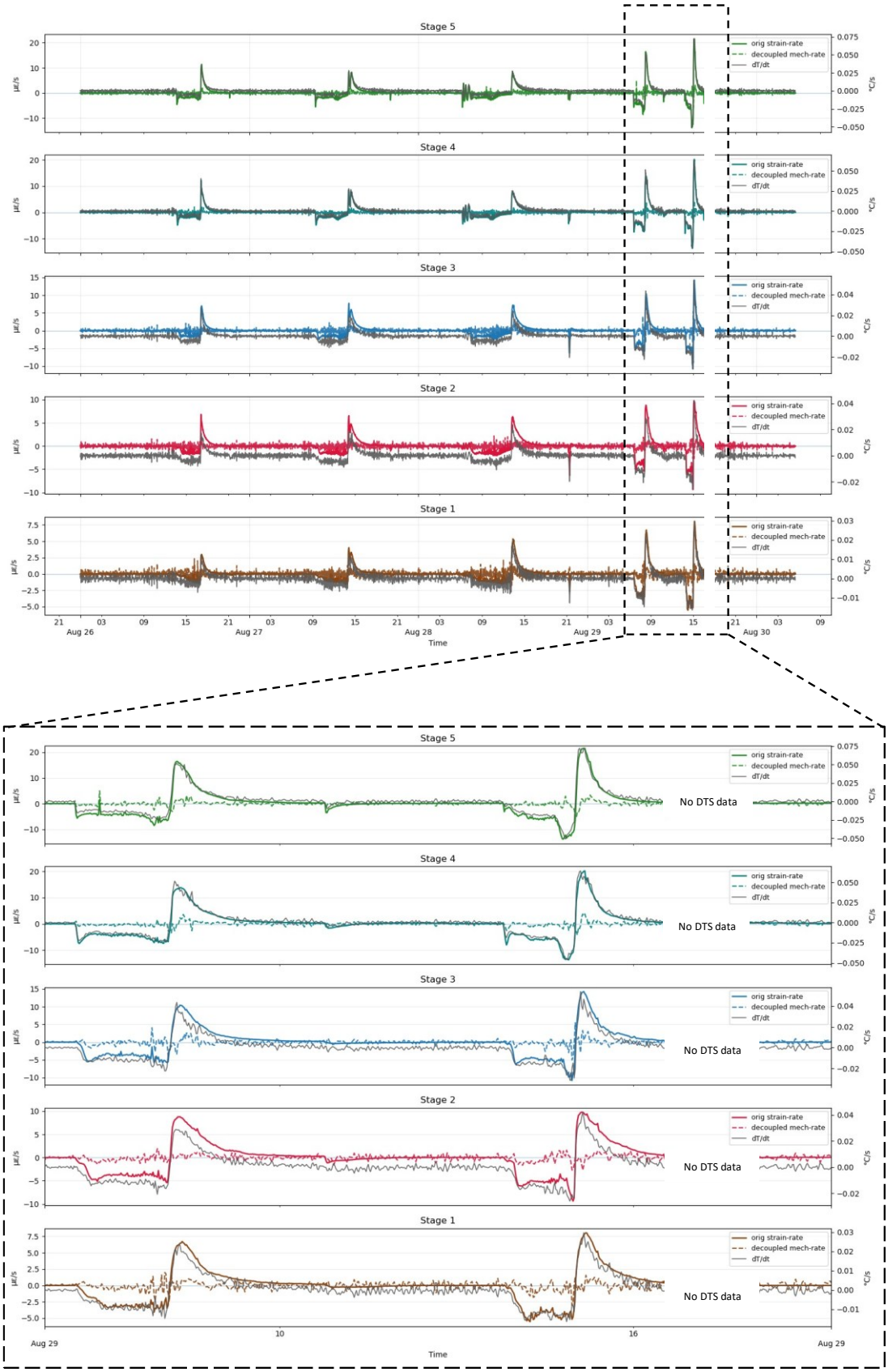

Figure 8: Average strain rate, temperature derivative and decoupled mechanical strain per stage.

Significantly, even though the mechanical-strain may not be clearly and unambiguously present in the data, the temperature-dominated portion of the RFS-DSS response is still highly informative. Temperature changes during flowback, tracked through the RFS DSS strain change, revealed inflow concentrated at specific stages/perforation intervals, and the shut-in temperature trend indicated inter-stage flow (Figure 9). Importantly, flow detected and measured during shut in periods indicates cross-flow between perforations, indicating that perforations connect to hydraulically separated fracture sets that are pressured differentially during injection and backflow. These behaviors are observed also in the DTS data, but the better spatial and temporal sampling resolution of the RFS-DSS produce much clearer signatures in the data.

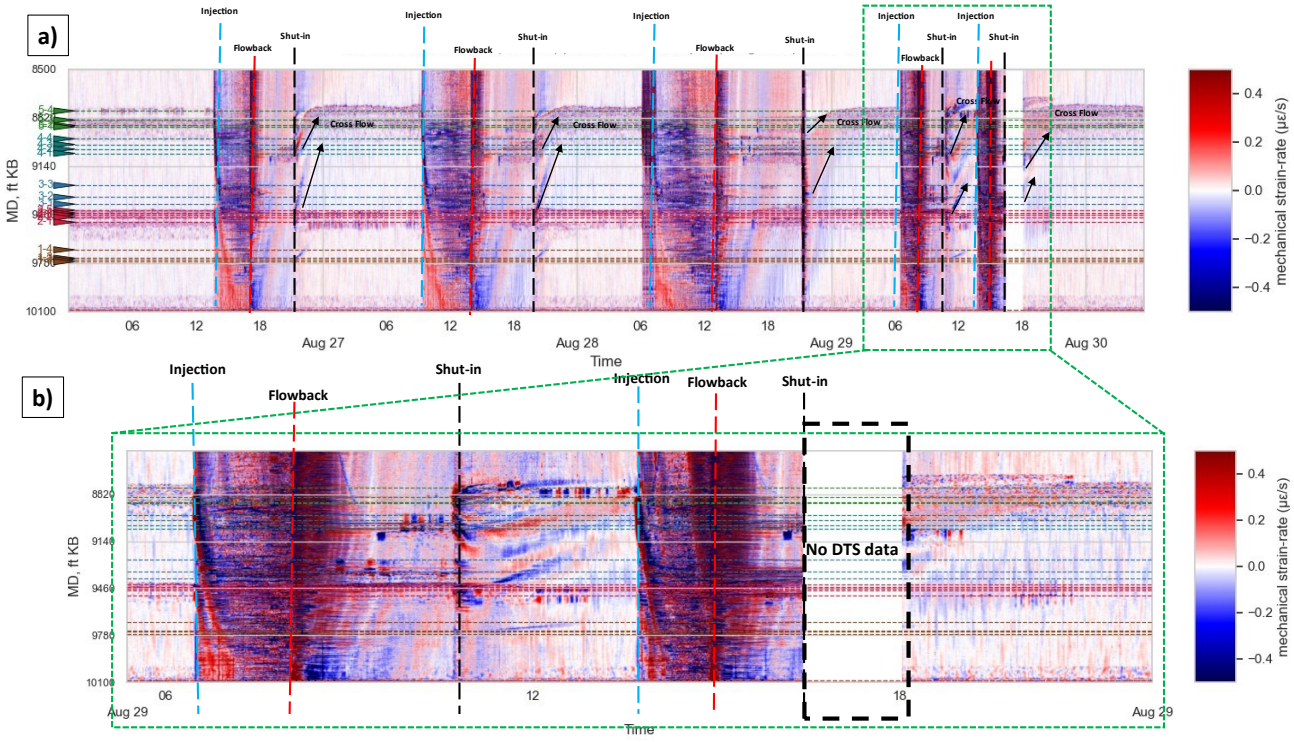

Figure 9: a) Decoupled mechanical strain, b) detailed view of the last two cycles. Zones where cross-flow was observed during shut-in periods are indicated by arrows showing the interpreted direction of fluid movement.

5. CONCLUSIONS

The RFS-DSS analysis shows that temperature cross-sensitivity dominates the apparent strain response during huff-and-puff operations. A DTS-measured temperature-informed separation approach was used to generate a residual signal, but the residual cannot yet be defended as true formation mechanical strain. If a mechanical strain signature is present in the RFS-DSS data, it is at least an order-of-magnitude smaller than the thermally induced strain signature. Apparent strain measured by RFS-DSS occurs due both to thermal elongation/contraction and consequent changes to the refractive index of the fiber glass along the continuous fiber strand in the tube inside the CT.

The apparent lack of a mechanical strain signature in the RFS-DSS data is not surprising. The dilation of a fracture during injection, for instance, must propagate from the formation, through cement, the steel production casing, the coiled tubing assembly loose in the casing, the capillary tubing loose in the coiled tubing, and finally through the fiber cable construction and finally onto the fiber glass itself. Of these, the slippage between the coiled tubing and casing, and the capillary tubes and the coiled tubing, are probably the most limiting. Similar issues have been identified for disposable intervention fiber deployed in casing (Song et al., 2024, 2025). Stick-slip friction is expected to occur even in this simpler deployment.

Coiled tubing deployment is attractive in geothermal applications due to the potential for fiber optic cable damage during deployment and recovery. An intervention cable composed of a heavy cable led by a passive traveler was deployed in this same well in August of 2024. This cable became stuck and then broke, fouling the well for many months. Coiled tubing deployments are more robust, but solutions must be found to better couple fiber to the coiled tubing and perhaps the coiled tubing to the casing.

Regardless of mechanical coupling issues, thermal gradients may accompany pressure gradients, and therefore strain changes during hydraulic testing. This issue is less problematic in multi-well tests because pressure propagates more rapidly than thermal signatures. In single well tests separation of temperature and strain effects cannot be avoided. Strain measurements (RFS DSS or DAS) should always be paired with a robust independent temperature measurement, preferably Ramen-based DTS. As shown here, differences in resolution

of temperature measurements and resolution, as well as differences in temporal and spatial sampling, can complicate the removal of temperature signature from strain with the objective of deriving the mechanical strain component from the RFS DSS strain data.

ACKNOWLEDGEMENTS

Work carried out for research at the Utah Frontier Observatory for Research in Geothermal Energy (FORGE) was funded in part by the US Department of Energy under DE-EE0007080 through the University of Utah (8-3617). We worked closely with Texas Tech University on the development of these field experiments, and we greatly appreciate the help the field support from FORGE staff Kevin England and Leroy Swearingen. We also thank Garret Maloney, a Master's student at CSULB, who also provided field support during these experiments.

REFERENCES

Ajo-Franklin, J., Becker, M., Chamarczuk, M., Coleman, T., Correa, J., Freifeld, B., Kim, J., Ghassemi, A., Ma, Y., & Maldaner, C. (2025). Distributed fiber-optic sensing deployment in a deep EGS production well at Utah FORGE: Preliminary results and lessons learned. *50th Workshop on Geothermal Reservoir Engineering, Stanford, CA*.

Department of Energy. (2023). https://www.energy.gov/eere/geothermal/forge-rd

Ghergut, I., Sauter, M., Behrens, H., Licha, T., McDermott, C. I., Herfort, M., Rose, P., Zimmermann, G., Orzol, J., & Jung, R. (2007). Tracer tests evaluating hydraulic stimulation at deep geothermal reservoirs in Germany. *Proceedings*.

LeBlanc, M., Song, X., Cox, C., & Byrd, D. (2025). Optimizing Fiber-Casing Coupling Efficiency for Horizontal Wellbores: A Lab-Scale Investigation Towards Improving Strain Measurements Using Disposable Fiber. *SPE Hydraulic Fracturing Technology Conference and Exhibition*, D021S006R007.

Liu, T., Li, Q., Li, X., Tan, Y., & Cao, X. (2024). A critical review of distributed fiber optic sensing applied to geologic carbon dioxide storage. *Greenhouse Gases: Science and Technology*, *14*(4), 676–694.

Pedraza, A., Del Río, D., Bautista-Juzgado, V., Fernández-López, A., & Sanz-Andrés, Á. (2023). Study of the Feasibility of Decoupling Temperature and Strain from a ϕ-PA-OFDR over an SMF Using Neural Networks. *Sensors*, *23*(12), 5515.

Pruess, K. (2010). *Thermal single-well injection-withdrawal tracer tests for determining fracture-matrix heat transfer area*.

Ratnayake, R., & Ghassemi, A. (2023). Modeling of Distributed Strain Sensing (DSS) in Utah FORGE Stimulations. *48th Workshop on Geothermal Resevoir Engineering*, 1–9.

Schölderle, F., Pfrang, D., & Zosseder, K. (2023). Inverse flow zone characterization using distributed temperature sensing in a deep geothermal production well located in the Southern German Molasse Basin. *Advances in Geosciences*, *58*, 101–108.

Sidenko, E., Tertyshnikov, K., Lebedev, M., & Pevzner, R. (2022). Experimental study of temperature change effect on distributed acoustic sensing continuous measurements. *Geophysics*, *87*(3), D111–D122.

Song, X., Jin, G., & Wu, K. (2024). Deciphering Cross-Well Strain Data from Single-Use Fiber with Slippage Effects During Fracturing. *SPE/AAPG/SEG Unconventional Resources Technology Conference*, D011S008R002.

Song, X., Jin, G., Wu, K., Pelton, K., & Ingle, T. (2025). Field Data Interpretation of Cross-Well Strain Measurements with Slippage Effect Using Single-Use Fiber in the Anadarko Basin. *SPE Hydraulic Fracturing Technology Conference and Exhibition*, D021S006R006.

Ugueto, G. A., Wojtaszek, M., Mondal, S., Guzik, A., Jurick, D., & Jin, G. (2021). New fracture diagnostic tool for unconventionals: high-resolution distributed strain sensing via Rayleigh frequency shift during production in hydraulic fracture test 2. *SPE/AAPG/SEG Unconventional Resources Technology Conference*, D021S031R002.

Xing, P., England, K., Moore, J., & McLennan, J. (2025). Analysis of the 2024 Circulation Tests at Utah FORGE and the Response of Fiber Optic Sensing Data. *50th Workshop on Geothermal Reservoir Engineering, Stanford University, Stanford, California*.

Zhou, D.-P., Li, W., Chen, L., & Bao, X. (2013). Distributed temperature and strain discrimination with stimulated Brillouin scattering and Rayleigh backscatter in an optical fiber. *Sensors*, *13*(2), 1836–1845.